

See discussions, stats, and author profiles for this publication at: <https://www.researchgate.net/publication/240475472>

Transition Metal Substitution in ETS10: DFT Calculations and a Simple Model for Electronic Structure Prediction

ARTICLE *in* CHEMISTRY OF MATERIALS · APRIL 2009

Impact Factor: 8.35 · DOI: 10.1021/cm8021177

CITATIONS

13

READS

26

3 AUTHORS, INCLUDING:



Babatunde A Ogunnaike

University of Delaware

203 PUBLICATIONS 2,250 CITATIONS

SEE PROFILE

Transition Metal Substitution in ETS-10: DFT Calculations and a Simple Model for Electronic Structure Prediction

Anne Marie Shough and Douglas J. Doren*

Department of Chemistry and Biochemistry, University of Delaware, Newark, Delaware 19716

Babatunde Ogunnaike

Department of Chemical Engineering, University of Delaware, Newark, Delaware 19716

Received August 1, 2008. Revised Manuscript Received January 11, 2009

The effects of transition metal substitution on the electronic structure of ETS-10 are elucidated for a variety of transition metal substituents (V^{IV} , V^V , Nb^V , Mo^V , Cr^{III} , Fe^{III} , and Cu^{II}) using density functional theory (DFT) and embedded cluster models. Properties intrinsic to the substituted metals (such as ionic radius and the number of d electrons) have been used to explain the energy changes observed for the valence and conduction bands and midgap states. Linear combinations of the key factors that control the energy of these electronic states have been developed that are capable of approximating the electronic structure for a variety of transition metal combinations substituted into the O–M–O chain of ETS-10. While not as accurate as DFT calculations, these electronic structure prediction models may be used to exhaustively search all possible transition metal combinations in a fraction of the time that it would take to investigate each system individually, using DFT. This inexpensive method allows for the preliminary identification of transition metal combinations that may be incorporated into the ETS-10 structure to improve its overall photocatalytic properties. An application of the electronic structure prediction models is also presented identifying transition metal combinations that may improve charge separation and decrease the band gap of ETS-10, thus improving the overall photocatalytic activity of this material.

1. Introduction

A variety of models have been developed in order to understand and predict the electronic structures of transition metal oxides. One of the most basic is ligand field theory,^{1,2} a local ionic model that describes how the electronic structures of d^n transition metal ions are perturbed as their environment changes. Although limited, this theory is useful for making approximate predictions of ground-state and excited-state electronic structures as well as for determining band gap energies and charge trapping states. Cluster models, treated with molecular orbital theory,^{2–4} are also local in nature, but improve upon ligand field theory by including the electronic interactions for a small group of atoms. Band theory is a more delocalized picture where the electronic interactions are considered for a periodic lattice.^{2,4} These theories may be used to identify optimal compositions and dopant materials that may improve the properties of transition metal oxides for specific applications.

In the field of photocatalysis, these theories have been applied to identify TiO_2 -based materials that are capable of

using solar energy.^{5–8} TiO_2 materials doped with transition metals⁹ and main group ions,^{10–12} result in a decreased optical band gap energy. However, many of these dopant centers can also serve as recombination centers, increasing the rate of electron–hole pair recombination, and decreasing the overall photocatalytic efficiency.¹³ Additionally, some transition metals are not easily incorporated into TiO_2 , limiting the choices for dopants.

ETS-10 is a microporous titanasilicate containing O–Ti–O chains that form lines of corner-sharing TiO_6 octahedra embedded in a SiO_2 framework (Figure 1a).^{14,15} Even though its photocatalytic properties are similar to those of TiO_2 , the chemical structure of ETS-10 is more flexible, facilitating the incorporation of a wider range of dopants. The chains

* Corresponding author. Tel: (302) 831-1070; Fax: (302) 831-6335. E-mail: doren@udel.edu.

- (1) Shriver, D. F.; Atkins, P.; Langford, C. H. *Inorg. Chem.*, 2nd Edition ed.; W. H. Freeman and Company: New York, 1994.
- (2) Cox, P. A. *Transition Metal Oxides: An Introduction to their Electronic Structure and Properties*; Oxford University Press: New York, 1992.
- (3) March, N. H. *Orbital Theories of Molecules and Solids*; Clarendon Press: Oxford, 1974.
- (4) Lowe, J. P. *Quantum Chemistry*; Academic Press Limited: London, 1993.

- (5) Umebayashi, T.; Yamaki, T.; Itoh, H.; Asai, K. *J. Phys. Chem. Solids* **2002**, *63*, 1909.
- (6) Zhang, Y.; Tang, C. Q.; Dai, J. *Acta Phys. Sin.* **2005**, *54*, 323.
- (7) Wang, H.; Lewis, J. P. *J. Phys. Condens. Mater.* **2005**, *17*, L209.
- (8) Nambu, A.; Graciani, J.; Rodriguez, J. A.; Wu, Q.; Fujita, E.; Sanz, J. F. *J. Chem. Phys.* **2006**, *125*, 094706.
- (9) Thompson, T. L.; Yates, J. J. *Top. Catal.* **2005**, *35*, 197.
- (10) Asahi, R.; Morikawa, T.; Ohwaki, T.; Aoki, K.; Taga, Y. *Science* **2001**, *293*, 269.
- (11) Morikawa, T.; Asahi, R.; Ohwaki, T.; Aoki, K.; Taga, Y. *Jpn. J. Appl. Phys.* **2001**, *40*, L561.
- (12) Burda, C.; Lou, Y.; Chen, X.; Samia, A. C. S.; Stout, J.; Gole, J. L. *Nano Lett.* **2003**, *3*, 1049.
- (13) Dvoranova, D.; Brezova, V.; Mazur, M.; Malati, M. A. *Appl. Catal., B* **2002**, *37*, 91.
- (14) Anderson, M. W.; Terasaki, O.; Ohsuna, T.; Philippou, A.; MacKay, S. P.; Ferreira, A.; Rocha, J.; Lidin, S. *Nature* **1994**, *367*, 347.
- (15) Anderson, M. W.; Terasaki, O.; Ohsuna, T.; Malley, P. J. O.; Philippou, A.; MacKay, S. P.; Ferreira, A.; Rocha, J.; Lidin, S. *Philos. Mag. B* **1995**, *71*, 813.

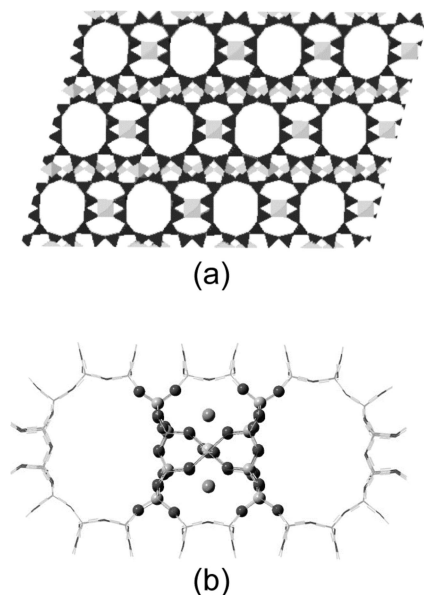


Figure 1. ETS-10. (a) Polymorph B polyhedral representation: TiO_6 , light gray; O_4 , dark gray;. (b) 3 M ONIOM model: QM region shown in ball and stick form; MM region shown in stick form.

of O—Ti—O behave as one-dimensional semiconducting wires insulated by a SiO_2 shell.^{16,17} The highly insulating SiO_2 framework makes the potential for electrons outside the O—Ti—O chain very large, so that the local geometric and electronic structures of the O—Ti—O wire dominate the optical properties of this material.^{16,17} Similar to TiO_2 , the optical band gap transition in ETS-10 is an $\text{O}(2p) \rightarrow \text{Ti}(3d)$ transition.^{18,19} The experimental band gap energy of ETS-10 is ~ 4.03 eV,^{16,17} which is blue-shifted from that of TiO_2 (~ 3.02 eV). This blue-shift has been attributed to quantum confinement in the radial direction of the O—Ti—O wire.^{16,17}

ETS-10 has been shown to photodegrade various organic pollutants^{20–23} and because of its porous nature can selectively photodegrade substrates based on size or shape.^{24,25} ETS-10 has been doped with various transition metals^{22,26–28} and main group metals^{29–31} to enhance its catalytic and

photocatalytic properties. This metal substitution may occur in either the tetrahedral Si or octahedral Ti sites. For example, Co(II) substitutes into the tetrahedral Si sites adjacent to the Ti—O—Ti—O chain and shifts the band gap of ETS-10 to lower energies.³² Additionally, ETCoS-10 materials have been shown to decompose acetaldehyde under visible light and have a higher photocatalytic activity than unmodified ETS-10.²² On the other hand, Cr(III) ,³³ Nb(V) ,²⁷ and Fe(III) ^{34,35} substitute in the octahedral Ti^{IV} sites. Both ETCrS-10 and ETNbS-10 display a slight increase in the catalytic activity for the dehydration of *tert*-butanol with a decreased selectivity for isobutene.^{27,33}

The substitution of V(IV) and V(V) into the octahedral sites of ETS-10 appears especially useful and displays activity for reactions where ETS-10 is inactive.^{23,28,36,37} V-substituted ETS-10 is also unique in that it is possible, using vanadium oxides in place of TiO_2 during synthesis, to create a pure vanadium form of ETS-10 (containing no titanium) known as AM-6.³⁷ The electronic structure of V-substituted ETS-10 at high V concentration demonstrates band gap energies within the visible range of the spectrum.³⁸ Additionally, at high [V], the band gap energy and presence of low energy electron traps can be controlled by the relative concentration of V^{IV} and V^{V} along the O—M—O chain, establishing V-substituted ETS-10 as a promising visible light photocatalyst.³⁸

This data shows that incorporating metals into the framework of ETS-10 can improve specific properties. With the exception of V substitution,³⁸ the effects of transition metal dopants on the structure of ETS-10 are not well understood. Without this information it is difficult to identify the optimal composition of ETS-10 for photocatalysis. By elucidating the trends that occur upon transition metal substitution into the one-dimensional chains of ETS-10, an attempt can be made to improve the properties of this material systematically for photocatalysis.

In the present work, we employ hybrid QM:MM cluster models and the fundamentals of ligand field theory to identify the electronic structure trends that occur when V^{V} , Nb^{V} , Mo^{V} , V^{IV} , Cr^{III} , Fe^{III} , and Cu^{II} are substituted into the octahedral Ti sites of ETS-10. The key factors that guide these trends are elucidated and incorporated into statistical models that allow the prediction of key states in the resulting electronic structure upon different transition metal substitutions. These models provide an inexpensive method for the preliminary identification of transition metal combinations that may be

- (16) Borello, E.; Lamberti, C.; Bordiga, S.; Zecchina, A.; Areat, C. O. *Appl. Phys. Lett.* **1997**, 71, 2319.
- (17) Lamberti, C. *Microporous Mesoporous Mater.* **1999**, 30, 155.
- (18) Xu, Y.-N.; Ching, W. Y.; Gu, Z.-Q. *Ferroelectrics* **1997**, 194, 219.
- (19) Ching, W. Y.; Xu, Y.-N.; Gu, Z.-Q. *Phys. Rev. B* **1996**, 54, 15585.
- (20) Krisnandi, Y. K.; Southon, P. D.; Adesina, A. A.; Howe, R. F. *Int. J. Photoenergy* **2003**, 5, 131.
- (21) Valente, A.; Lin, A.; Brandao, P.; Portugal, I.; Anderson, M. W.; Rocha, J. *J. Catal.* **2001**, 200, 99.
- (22) Uma, S.; Rodrigues, S.; Martyanov, I. N.; Klabunde, K. J. *Microporous Mesoporous Mater.* **2004**, 67, 181.
- (23) Philippou, A.; Naderi, M.; Rocha, J.; Anderson, M. W. *Catal. Lett.* **1998**, 53, 221.
- (24) Calza, P.; Paze, C.; Pelizzetti, E.; Zecchina, A. *Chem. Commun.* **2001**, 2130.
- (25) Llabres i Xamena, F. X.; Calza, P.; Lamberti, C.; Prestipino, C.; Damin, A.; Bordiga, S.; Pelizzetti, E.; Zecchina, A. *J. Am. Chem. Soc.* **2003**, 125, 2264.
- (26) Brandao, P.; Philippou, A.; Valente, A.; Rocha, J.; Anderson, M. W. *Phys. Chem. Chem. Phys.* **2001**, 3, 1773.
- (27) Rocha, J.; Brandao, P.; de Jesus, J. D. P.; Philippou, A.; Anderson, M. W. *Chem. Commun.* **1999**, 471.
- (28) Brandao, P.; Valente, A.; Tocha, J.; Anderson, M. W. *Stud. Surf. Sci. Catal.* **2002**, 142, 327.
- (29) Anderson, M. W.; Philippou, A.; Lin, Z.; Ferreira, A.; Rocha, J. *Angew. Chem., Int. Ed.* **1995**, 34, 1003.
- (30) Anderson, M. W.; Rocha, J.; Lin, A.; Philippou, A.; Orion, I.; Ferreira, A. *Microporous Mater.* **1996**, 6, 195.

- (31) Rocha, J.; Lin, Z.; Ferreira, A.; Anderson, M. W. *J. Chem. Soc. Chem. Commun.* **1995**, 867.
- (32) Eldewik, A.; Howe, R. F. *Microporous Mesoporous Mater.* **2001**, 48, 65.
- (33) Brandao, P.; Philippou, A.; Valente, A.; Rocha, J.; Anderson, M. W. *Phys. Chem. Chem. Phys.* **2001**, 3, 1773.
- (34) Lazar, K.; Das, T. K.; Chaudhari, K.; Chandwadkar, A. J. *Stud. Surf. Sci. Catal.* **1999**, 125, 301.
- (35) Lazar, K.; Chandwadkar, A. J.; Fejes, P.; Cejka, J.; Ramaswamy, A. V. *J. Radioanal. Nucl. Chem.* **2000**, 246, 143.
- (36) Catanzaro, L.; De Luca, P.; Nagy, J. B.; Nastro, A. *Stud. Surf. Sci. Catal.* **2004**, 154, 746.
- (37) Rocha, J.; Brandao, P.; Lin, Z.; Anderson, M. W.; Alfredsson, V.; Terasaki, O. *Angew. Chem., Int. Ed.* **1997**, 36, 100.
- (38) Shough, A. M.; Doren, D. J.; Lobo, R. F. *Phys. Chem. Chem. Phys.* **2007**, 9, 5096.

incorporated into the ETS-10 structure in order to improve the overall photocatalytic properties of the material. These results may then be used to guide more computationally and experimentally extensive analyses.

2. Computational Methods

All models have been derived from the 3 M ONIOM model previously used to represent pure ETS-10 and V^{IV}- and V^V-substituted ETS-10 (Figure 1b).^{38–40} These systems contain a single O–M–O chain incorporating three metal (M) sites surrounded by the immediate SiO₂ framework, and are optimized using a mixed density functional theory/molecular mechanics (DFT/MM) method, where the PBE⁴¹ functional is used to describe the DFT region. We have previously demonstrated that band gap energy differences between two finite O–Ti–O chains containing three and five Ti atoms and an infinitely long O–Ti–O chain are negligible.³⁹ As such we are able to investigate the optical properties of this three Ti system without concern for any significant optical confinement in the axial direction of the O–Ti–O chain. Additionally, the geometries and electronic structures of the ETS-10 and V-substituted models are consistent with experimental data, supporting the use of this model for the investigation of a variety of transition metal substitutions. The set of geometric models includes the parent ETS-10 model as well as models substituted with V^{IV}, V^V, Nb^V, Mo^V, Cr^{III}, Fe^{III}, and Cu^{II}. Models include one, two, and/or three substituted metal atoms in order to investigate the effects of varying concentration, for a total of 23 mono- and [M/Ti] bimetallic systems. A list of all structural models and details on computational methods can be found in Table S1 and Section S1, respectively, in the Supporting Information.

3. Results and Discussion

3.1. Trends in M/Ti Bi-Metallic Systems. The three metal sites in the cluster models allow for transition metal substitution at varying concentrations. Models have been developed at 33, 66, and 100% substitution for V^{IV}, V^V, Nb^V, and Mo^V. Only 33% and 66% substituted models were found to be stable for Cr^{III} and Fe^{III} substitution, and only a 33% substituted model was identified for Cu^{II}. Unlike the +4 and +5 metals, these lower oxidation state metals require additional counter-ions in the large channels to achieve charge neutrality. This suggests that the ETS-10 structure is unstable when a high concentration of counterions is present in the large channels. This limits the substitution of these metals (Fe^{III}, Cr^{III} and Cu^{II}) to low concentrations.

Trends for transition metal substitution into the geometric structure of ETS-10 are discussed in section 3.1.1. The quantum chemical results are discussed in the framework of ligand field theory, to understand how changes in atomic properties relate to changes in electronic energies, with regard to the d orbitals (section 3.1.2), the valence band (section 3.1.3), the conduction band (section 3.1.4), and midgap charge trapping states (section 3.1.5). Because of the fact that the number of occupied d-orbitals largely controls the band structure, most of the discussions pertaining to elec-

tronic structure trends are divided into groups of different *dⁿ* metals. This allows for the elucidation of trends within transition metal subgroups.

3.1.1. Geometries. The metal ions are in a distorted octahedral coordination where the M–O_a bonds are shorter in length than the M–O_{eq} bonds. The average M–O (a, axial; eq, equatorial) bond lengths for a specified metal in the 23 optimized mono- and [M/Ti] bimetallic model geometries are reported in Table S2 of the Supporting Information. For the metal ions with ionic radii⁴² ranging from 0.54–0.73 Å, the central M–O_a bonds change by only ~0.1 Å, indicating that the axis of the O–M–O chain is highly constrained. This suggests that relaxation around the substituted metal ions primarily occurs in the radial direction of the O–M–O chain. Table S2 shows that the average bulk M–O_{eq} bond changes by ~0.4 Å across all substituted metals, consistent with a more flexible structure in the radial direction. The difference between the M–O_a and M–O_{eq} bond distances is larger for metal ions substituted into the central bulk position (M2) than into the surface/end positions (M1, M3).

We also find that the counterion environment influences the symmetry of the chain axis. As reported previously,⁴⁰ there exists a chain asymmetry (one short and one long M–O_a bond) surrounding each V^V site upon V^V substitution. This asymmetry becomes more pronounced as the number of adjacent V^V sites is increased, and has been attributed⁴⁰ to a combination of the required removal of Na counterions from the structure of ETS-10 and the small ionic radius of V^V. Nb^V and Mo^V substitution also require the removal of Na counterions, resulting in a similar chain asymmetry. However, the asymmetry is not as severe for these metals because of the larger ionic radii of Nb^V and Mo^V as compared to V^V. A similar chain asymmetry is also observed for substitution of Cr^{III}, Fe^{III}, and Cu^{II}, which require counterions to be added into the large channels. This suggests that both ionic radii and cation environment surrounding a given metal ion are important factors in determining the local MO₆ geometry for a given metal.

3.1.2. d Orbitals. In a distorted octahedral geometry, the d-orbitals of the metal centers of ETS-10 are split farther beyond the standard octahedral splitting, Δ_O, between the e_g and t_{2g} orbitals (Figure 2). In ligand field theory, the d_{xz}, d_{yz}, and d_{z²} orbitals, which have lobes directed along the chain axis (z-axis), are destabilized due to the shortening of the M–O_a bonds, while the d_{xy} and d_{x² – y²} orbital, which have only x and y character, are in turn stabilized (Figure 2). This additional splitting within the t_{2g} and e_g orbitals, arising from the distortion of the octahedral coordination, will be referred to as Δ_{dist}.

As transition metals are substituted into the O–M–O chain, the amount of mixing between the d orbitals of neighboring metal ions depends on two main factors. The first is the relative d-orbital energies of the two metals. In general, transition metal d-orbital energies decrease across a row of the periodic table. However the energies of the d orbitals also depend on the amount of d-orbital splitting, Δ_O and Δ_{dist}. As the metal–ligand interaction increases, which

(39) Zimmerman, A. M.; Doren, D. J.; Lobo, R. F. *J. Phys. Chem. B* **2006**, *110*, 8959.

(40) Shough, A. M.; Doren, D. J.; Lobo, R. F.; Nash, M. *J. Phys. Chem. C* **2007**, *111*, 1776.

(41) Perdew, J. P.; Burke, K.; Ernzerhof, M. *Phys. Rev. Lett.* **1996**, *77*, 3865.

(42) Lide, D. *CRC Handbook of Chemistry and Physics*; CRC Press: Boca Raton, FL, 2001–2002.

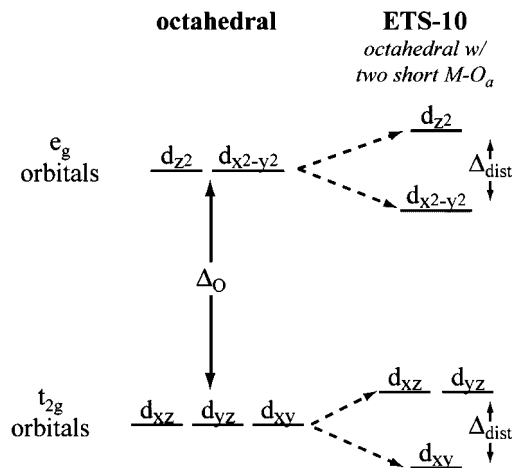


Figure 2. Crystal field splitting between the t_{2g} and e_g d orbitals of a transition metal oxide in perfect octahedral coordination, Δ_O , is illustrated on the left side of the figure. The additional splitting, Δ_{dist} , within the t_{2g} and e_g orbitals because of a distorted octahedral coordination where two M–O bonds are shorter than the rest is shown on the right side of the figure.

occurs with increasing oxidation state and decreasing ionic radii, the octahedral splitting, Δ_O , between the t_{2g} and e_g orbital increases. The difference in M–O bond distances between the axial and equatorial bonds also affects the energies of the d orbitals. As the M–O_{eq} bonds become longer and/or the M–O_a bonds shorter, the splitting within the t_{2g} and e_g orbitals, Δ_{dist} , also increases (Figure 2). Shorter M–O_a bonds and longer M–O_{eq} bonds are observed when the metal ions are substituted into the bulk (central) site versus one of the surface (chain end) sites (see Table S2 in the Supporting Information). This increases Δ_O and Δ_{dist} when a metal is substituted into a bulk site, significantly lowering the energy of the d_{xy} state.

Assuming that the difference in d-orbital energies between the metals is not large, orbital mixing is then determined by the amount of orbital overlap. Because of the linear arrangement of the metal ions in the ETS-10 structure, only the d-orbitals with lobes in the direction of the chain axis (z-axis) have a significant orbital overlap.³⁸ Therefore the d_{xz} , d_{yz} , and d_z states are delocalized across all metal sites in the O–M–O chain, and the energies of the resulting MO's depend on the individual d-orbital energies of all three metals.

However, for the d orbitals having lobes in the equatorial direction only (i.e., d_{xy} and $d_{x^2-y^2}$) the amount of orbital overlap is insignificant and thus orbital mixing between neighboring metals does not occur. This results in localized MOs that are dominated by d_{xy} or $d_{x^2-y^2}$ character of a single metal center. The absolute energy of these localized states is governed by the d-orbital energies and the local MO₆ geometry of a given metal, and is not largely affected by neighboring metals. Yet the relative position of these localized states with respect to the top of the valence band (VB) and the bottom of the conduction band (CB) is dependent on the neighboring metal ions, because the VB and CB are delocalized states whose energies depend on the entire chain system. When the d-orbital energies of neighboring MO₆ groups differ significantly, localized d_{xy} and $d_{x^2-y^2}$ orbitals may be located far above the VB or below the CB, and thus within the band gap. These midgap states may result

in hole or electron trapping sites along the O–M–O chain depending on whether these states are occupied or unoccupied, respectively. The trends of these localized states and their impact on the photocatalytic activity of ETS-10 will be discussed in more detail in section 3.1.5.

3.1.3. Valence Band. Although the models used in the present work are finite clusters with discrete states, for simplicity we have defined the top of the valence band (VB) to be the highest occupied molecular orbital (HOMO) positioned less than 0.5 eV above the next highest MO. Similarly, the bottom of the conduction band (CB) is defined as the lowest unoccupied molecular orbital (LUMO) positioned less than 0.5 eV below the next lowest MO. This allows for states within the VB and CB to be differentiated from occupied or unoccupied states that may be located within the band gap, thus serving as potential charge trapping states.

In most models, midgap states are positioned >1 eV away from the top of the valence band (or bottom of the conduction band), making their classification as “midgap states” more certain. However, as will be discussed below, low-lying occupied (or high-lying unoccupied) midgap states are predicted in the Fe models, which are <1 eV from the top of the VB (or bottom of the CB). In these models, the distinction between states embedded in bands and states within the band gap become less certain. Although tentative assignments are made, the investigation of periodic models and experimental studies would be needed to confirm the “classification” of these states.

3.1.3.1. d^{0-3} Metals: V^V, Nb^V, Mo^V, V^{IV}, Cr^{III}. For d^{0-3} substituted models, the top of the valence band resembles that of ETS-10 where the primary orbital contribution is comprised of the O(2p) orbitals of the axial O (Figure 3). As seen in the left panel of Figure 4, the energy of the highest occupied state dominated by O(2p) character, denoted $h\text{-O}(2p)$, is correlated with the average oxidation state of the metals present. The increasing positive charge on the metals, introduced by higher oxidation states, is compensated by an increasing negative charge on the O ligands. This results in lower energy O(2p) states.

3.1.3.2. d^{5-9} Metals: Fe^{III}, Cu^{II}. The correlation between the energy of the $h\text{-O}(2p)$ state and the averaged oxidation state of the metals in the model also holds true for d^5 Fe^{III} and d^9 Cu^{II} metal substitution (data included in left panel of Figure 4). However, in these systems the $h\text{-O}(2p)$ state is no longer the highest occupied state within the valence band (Figure 3). Instead, the top of the valence band is comprised of states dominated by metal d character. This difference can be attributed to two factors. First, these systems incorporate the highest number of d electrons of the transition metals investigated in this study, and electron occupation significantly lowers the energy of a MO. Second, atomic d-orbital energies decrease across a periodic row, so that the atomic d-orbital energies of Fe and Cu are the lowest of the transition metals considered in this study.

There are some differences between the valence bands of the Fe^{III} and Cu^{II} substituted models. For the Cu^{II} substituted system the energy difference between the localized

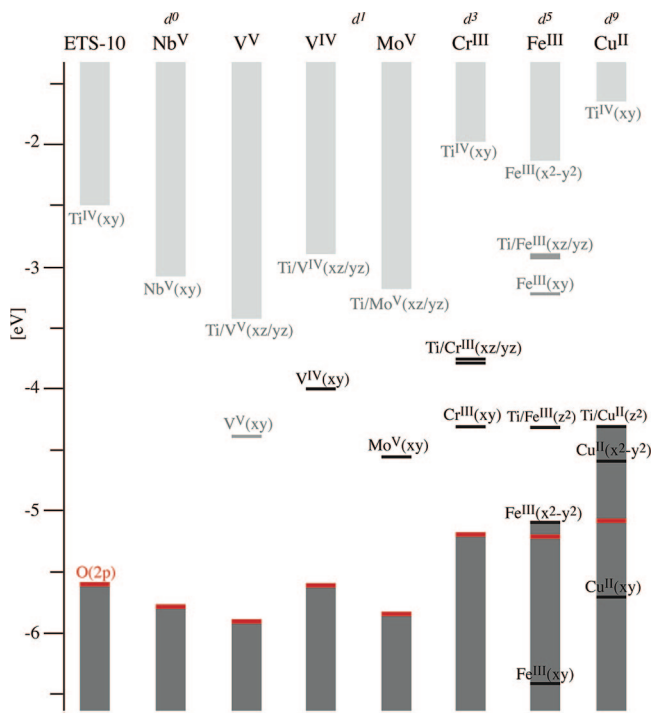


Figure 3. Comparison of electronic structures for ETS-10 and all 33% substituted [M/Ti] models estimated using DFT orbital energies. Position of h -O(2p) state shown in red. Unoccupied and occupied midgap states differentiated by black and gray lines, respectively. Unoccupied valence band and occupied conduction band states shown in light and dark gray rectangles, respectively.

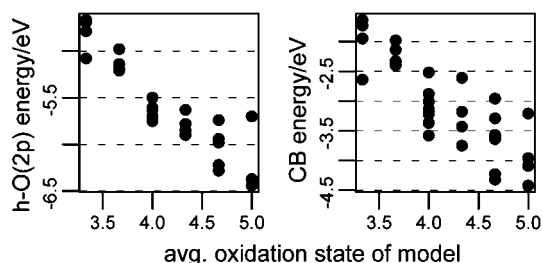


Figure 4. Energy dependence of the h -O(2p) state (left) and lowest unoccupied conduction band state (right) on the average oxidation state of all 23 mono- and [M/Ti] bimetallic 3 M ONIOM models.

$\text{Cu}^{\text{II}}(d_{x^2-y^2})$ and delocalized $\text{Cu}^{\text{II}}/\text{Ti}^{\text{IV}}(d_{z^2})$ states is ~ 0.3 eV, so that both of these states can be classified as valence band states (Figure 3). For Fe^{III} , the Δ_{dist} splitting between the $d_{x^2-y^2}$ and d_{z^2} states in the $\text{Fe}^{\text{III}}\text{O}_6$ distorted octahedra is larger, so that the $\text{Fe}^{\text{III}}/\text{Ti}^{\text{IV}}(d_{z^2})$ state is positioned ~ 0.5 – 0.8 eV above the top of the VB (Figure 3). On the basis of M–O bond distances alone, Cu^{II} would be expected to have a higher Δ_{dist} than Fe^{III} (see Table S2 in the Supporting Information). However the increased exchange energy in the high-spin d^5 Fe^{III} -substituted systems, may lead to a higher Δ_{dist} . This suggests that systems substituted with low concentrations of Fe^{III} may have low-lying hole trapping states that are delocalized along the metal d_{z^2} states.

3.1.4. Conduction Band. For all models investigated in the present work, metal d states dominate the bottom of the conduction band (Figure 3). The energy of these states therefore depends on the relative d-orbital energies of the metals, which in turn depend on the oxidation state and ionic

radii of these metals. The right panel of Figure 4 illustrates the strong correlation between the average oxidation state of the metals present in each model and the resulting CB energy. Additionally, d-orbital occupation lowers the energy of these d states, moving them away from the bottom of the CB, and indirectly lowering the unoccupied d states remaining in the CB. As a result, the energies of the unoccupied states at the bottom of the conduction band also depend on the total number of d-electrons in the system.

3.1.4.1. d^{0-1} Metals: V^{V} , Nb^{V} , Mo^{V} , V^{IV} . In the d^{0-1} bimetallic M/Ti $^{\text{IV}}$ systems, the bottom of the conduction band is typically comprised of a delocalized metal(d_{xz}/d_{yz}) state. The energy of this state reflects the MO_6 t_{2g} orbital energies of all the metals. With increasing oxidation state and decreasing ionic radii, the value of Δ_{O} increases, lowering the energy of the t_{2g} (d_{xy} , d_{xz} , and d_{yz}) orbitals. As can be seen in Figure 3, the greatest amount of CB lowering occurs upon V^{V} substitution, which has the smallest ionic radius and highest oxidation state of all the metals investigated.

The Nb^{V} substituted systems are one case where the bottom of the conduction band has a different electronic structure (Figure 3). The t_{2g} orbital energies of Nb^{V} are predicted to be slightly lower than those of Ti^{IV} . However, the difference between Nb^{V} and Ti^{IV} t_{2g} orbital energies is small that the localized $\text{Nb}^{\text{V}}(d_{xy})$ state appears just at the bottom of the conduction band (Figure 3).

3.1.4.2. d^{3-5} Metals: Cr^{III} , Fe^{III} . Substitution of the d^3 (Cr^{III}) and d^5 (Fe^{III}) metals investigated in the present work, lead to high spin state models with all d electrons having parallel spins. For these models, the lower edge of the conduction band is comprised of the unoccupied (minority spin) metal d-states. For Cr^{III} , the smaller oxidation state and similar ionic radius to Ti^{IV} results in a smaller Δ_{O} and higher energy unoccupied t_{2g} orbitals. Thus in the mixed $\text{Cr}^{\text{III}}/\text{Ti}^{\text{IV}}$ system the unoccupied (minority spin) delocalized $\text{Cr}^{\text{III}}/\text{Ti}^{\text{IV}}(d_{xz}/d_{yz})$ states are higher in energy than the unoccupied localized $\text{Ti}^{\text{IV}}(d_{xy})$ state that is positioned at the bottom of the CB (Figure 3).

With a smaller ionic radius, however, the unoccupied t_{2g} orbital energies of Fe^{III} are significantly lower than those of Cr^{III} and Ti^{IV} . At low $[\text{Fe}^{\text{III}}]$, the bottom of the CB comprises the localized unoccupied (minority spin) $\text{Fe}^{\text{III}}(d_{x^2-y^2})$ state, whereas the unoccupied (minority spin) $\text{Fe}^{\text{III}}(d_{xy})$ and $\text{Fe}^{\text{III}}/\text{Ti}^{\text{IV}}(d_{xz}/d_{yz})$ states are positioned ~ 0.7 eV below the bottom of the CB (Figure 3). This suggests that at low concentrations of Fe^{III} , the localized $\text{Fe}^{\text{III}}(d_{xy})$ and delocalized $\text{Fe}^{\text{III}}/\text{Ti}^{\text{IV}}(d_{xz}/d_{yz})$ states may serve as high-lying electron trapping sites.

3.1.4.3. d^9 Metal: Cu^{II} . Unlike the other transition metal substituted models, the d-band of the d^9 Cu^{II} substituted model is almost completely filled. As stated above, these filled states are positioned at the top of the valence band for Cu^{II} substituted systems. The minority spin delocalized $\text{Cu}^{\text{II}}/\text{Ti}^{\text{IV}}(d_{z^2})$ state, however, is unoccupied and positioned within the CB, whereas the state at the bottom of the CB is an unoccupied localized $\text{Ti}^{\text{IV}}(d_{xy})$ state.

3.1.5. Midgap Charge Trapping States. As noted in section 3.1.2, the geometry of the O–M–O chain only allows for orbital mixing between the d_{xz} , d_{yz} , and d_{z^2} states, while the d_{xy} and $d_{x^2-y^2}$ states remain localized on a single metal site.

The energies of the localized $M(d_{xy})$ and $M(d_{x^2-y^2})$ states are primarily determined by the d-orbital energies and the local MO_6 geometry for a given metal, while the energies of the delocalized d orbitals depend on the d-orbital energies for all metals along the O—M—O chain. If the d-orbital energies of the metals along the O—M—O chain are very different, the localized states are likely to be positioned within the band gap thus serving as potential charge trapping sites. Additionally, in some cases, if the difference in d-orbital energies between the individual metals is large, the energy of the resulting delocalized state may be lowered significantly below the bottom of the CB and may also be considered as a potential charge trapping state (see Figure 3).

Excluding the Fe^{III} models, the relative energies of the localized $M(d_{xy})$ states with respect to the VB and CB are a good indication of whether charge trapping sites will be present in the band gap. When localized $M(d_{xy})$ states are positioned in the band gap, localized/delocalized charge trapping states occur. Below we will identify the trends for the specific midgap states that occur within the subgroups of d^0 , d^{1-3} , and d^{5-9} metals paying particular attention to the energy of the localized d_{xy} state.

3.1.5.1. d^0 Metals: V^V , Nb^V . Upon d^0 metal substitution, all molecular orbitals dominated by metal d character are unoccupied. As noted above, the t_{2g} orbital energies of Nb^V are similar to those of Ti^{IV} , and localized $Nb^V(d_{xy})$ states are positioned at or near the bottom of the conduction band in Nb^V/Ti^{IV} systems. On the other hand, the smaller ionic radius of V^V has been shown to lead to a larger Δ_O and lower energy t_{2g} orbitals for the V^V states.³⁸ The large difference between the V^V and Ti^{IV} d-orbital energies results in localized $V^V(d_{xy})$ midgap states for all V^V/Ti^{IV} systems (Figure 3), which may serve as potential electron trapping states.

The presence of charge trapping sites can increase recombination rates and thus decrease the overall photocatalytic activity. However, the simultaneous presence of both electron and hole trapping sites may lead to improved charge separation depending on the relative position of the trapping sites. As such, we propose that V^V substitution can play a crucial role in improving the photocatalytic properties of ETS-10. Note that in some cases, where V^V is cosubstituted with late transition metals (Cr^{III} , Cu^{II} , Fe^{III}) that contribute a number of d electrons to the system, electron transfer may occur to the V^V center, resulting in a reduced oxidation state (i.e., V^{IV}).

3.1.5.2. d^{1-3} Metals: V^{IV} , Cr^{III} , Mo^V . Substitution with d^{1-3} metals (V^{IV} , Cr^{III} , Mo^V) allows for partial occupation of the t_{2g} orbitals. Both V^{IV} and Mo^V have larger values of Δ_O (i.e., lower t_{2g} orbital energies) than Ti^{IV} , because of smaller ionic radii and higher oxidation states, respectively. This positions the localized $V^{IV}(d_{xy})$ and $Mo^V(d_{xy})$ states below the bottom of the conduction band for M/Ti systems. Both of these metals also contribute a single d electron, which occupies the localized $M(d_{xy})$ midgap states. This lowers the energy of these states further and leads to possible hole trapping sites on the substituted metal centers (Figure 3).

The increasing number of d electrons introduced by Cr^{III} substitution leads to partial occupation of all of the Cr^{III} t_{2g}

orbitals. This lowers the energy of the occupied localized $Cr^{III}(d_{xy})$ and delocalized $Cr^{III}/Ti^{IV}(d_{xz}/d_{yz})$ states to lie within the band gap (Figure 3). Because photogenerated holes prefer states of higher energy, it is possible that in this system, a hole trapped in the localized $Cr^{III}(d_{xy})$ may easily transition into the more delocalized d_{xz}/d_{yz} state. Although these delocalized d_{xz}/d_{yz} states are far below (>1 eV) the bottom of the CB, they are delocalized across all metal sites and may be effective in transporting the photogenerated holes to the active sites of ETS-10. This interpretation depends somewhat on the model used. In extended systems, these states may act as hole traps, particularly if the metal substitution has little order.

3.1.5.3. d^{5-9} Metals. The Fe^{III} and Cu^{II} d orbitals are much lower in energy than those of the early transition metals. This is due to the lower energy of the atomic d orbitals of the late transition metals as well as the large number of occupied d states. As such, the occupied localized $Fe^{III}(d_{xy})$ and $Cu^{II}(d_{xy})$ states are positioned >1 eV below the top of the valence band and are unlikely candidates for charge trapping states.

The Cu^{II} substituted model, having a low concentration of Cu^{II} , displays no midgap states. In general midgap states are more likely for smaller dopant concentrations, suggesting that at higher concentrations of Cu^{II} substitution, midgap states will not occur. As discussed above, at low concentrations of Fe^{III} , the greater values of Δ_O and Δ_{dist} for Fe^{III} leads to potential hole trapping in delocalized $Fe^{III}/Ti^{IV}(d_{yz})$ states and electron trapping in localized $Fe^{III}(d_{xy})$ and delocalized $Fe^{III}/Ti^{IV}(d_{xz}/d_{yz})$ states. Note that these states are positioned <1 eV above the VB or below the CB. Because of the limitations of the finite cluster models here, these states are only tentatively identified as charge trapping states.

3.2. Simple Prediction Model. We have identified the trends in the energies of the VB, CB, and midgap states upon substitution of various transition metals into the ETS-10 system, along with the key factors that guide these trends. These discussions have been limited to mono- and [M/Ti] bimetallic systems only. To identify the optimal transition metal substitutions of ETS-10 for photocatalysis, we should consider all mono-, bi-, and trimetallic transition metal combinations in order to exploit the properties of each transition metal. Applying our quantum chemistry approach to each unique three-metal combination using the eight transition metals investigated in the present study would require vast computational resources and ultimately result in combinations that provide no improvement in photocatalytic activity.

We propose that by identifying intrinsic properties of the substituted metals that are the key factors in determining electronic energies of modified ETS-10, we can develop a simple model that can be used to estimate these energies in other systems. The goal is an approximate description of the band structure and midgap states that can be used to identify transition metal combinations capable of improving the photocatalytic properties of ETS-10. These combinations may then be probed with higher-level theoretical and experimental methods to gain more accurate insight into the properties of these transition metal combinations.

The first state considered is the h -O(2p) state. In most cases, this state is positioned at the top of the VB. For models incorporating late transition metals, however, the top of the VB comprises occupied d orbitals, whereas the h -O(2p) state is <1 eV below the top of the VB. Therefore, the energy of the h -O(2p) state is a good first approximation for the top of the VB. The h -O(2p) state is also important in determining the lowest ligand to metal charge transfer (LMCT) transition. Thus knowing the approximate energy of the h -O(2p) state is valuable. Finally, the energy trend for the h -O(2p) state is consistent for all substituted transition metal models, where the effective charge on the metal centers (as described by the metal ion oxidation states and counterion environment) is the key factor directing the energy of this state (section 3.1.3).

The second state is the bottom of the CB. For all substituted transition metals the states at the bottom of the CB are d-orbital states (section 3.1.4). Combined with the energy of the h -O(2p) state, the predicted CB energy is essential in predicting LMCT transition energies as well as in classifying any midgap charge trapping states that may be present. The energy of the d-orbital positioned at the bottom of the conduction band depends on the relative d-orbital energies of the metals coordinated along the O–M–O chain. The key factors affecting d-orbital energies are: (1) ionic radii, (2) effective charge (i.e., oxidation state and counterion environment), and (3) the number of d electrons.

The energy of the localized $M_i(d_{xy})$ state, for a given metal M_i , is the last state considered. In most cases, the relative energies of the localized $M_i(d_{xy})$ states with respect to the VB and CB indicate whether midgap states will be present. The energy of a localized $M_i(d_{xy})$ state is primarily controlled by the d-orbital energies of a given metal M_i , and is not significantly affected by neighboring metal ions. The key factors affecting d-orbital energies of a metal are (1) the metal ionic radius, (2) the effective charge on the metal (i.e., oxidation state and local counterion environment), (3) the number of occupied d orbitals, and (4) position along the O–M–O chain (i.e., bulk or surface site substitution).

3.2.1. Data Set and Variable Selection. The fitting data are taken from 30 optimized 3 M ONIOM cluster models, which includes the 23 mono- and [M/Ti] bi-metallic models used for the analysis presented in section 3.1, and 7 additional bi- and trimetallic models. The geometries of all 3 M ONIOM cluster models have been optimized using the DFT/MM methods described above (section 2). A complete list of the 30 structural models as well as the calculated energies used to fit the prediction models can be found in Table S1 of the Supporting Information. The model set is heavily weighted with early transition metal substituted models. For those models containing late transition metals (Fe^{III} and Cu^{II}), only small to moderate substitution concentrations have been considered (33–66%). As such, the validity of the prediction models developed in the present study may be limited to metal combinations incorporating only early transition metals or possibly low concentrations of late transition metals.

A set of 19 variables was initially considered to fit the data from the structural models, including intrinsic transition

metal ion properties such as oxidation state and ionic radii. For brevity, a detailed explanation of all variables can be found in the Supporting Information, section S2.1. To accommodate the high correlation that exists among these variables, we have employed partial least-squares (PLS) regression, which is able to deal with the problems created by excessive redundant descriptors and a small sample size.⁴³ The leave-one-out cross-validation (LOO-CV) method⁴⁴ has also been employed to calculate the root mean squared error of prediction (RMSEP) for each variable combination, which is used to identify the optimal number of components and minimize the amount of overfitting. All statistical analyses have been carried out using the R statistical environment.⁴⁵

The size of our data set is severely limited by the computational cost required to optimize a single 3 M ONIOM cluster model. As such, not all variables are normally distributed. PLS regression performed on such a biased data set will lead to an incorrect identification of variables and weights; the resulting model will also exhibit poor predictability for new systems. To ensure that the final variable set and the coefficient weights are unbiased, we have employed the bootstrap resampling method,⁴⁶ because of its usefulness in minimizing these types of biases. A detailed description of the bootstrap resampling parameters and the criteria for eliminating irrelevant descriptors can be found in the Supporting Information, sections S2.2 and S2.3.

3.2.2. Final Variable Set. The mean and standard deviations for the weights of the final variable sets for all three prediction models, as determined with the bootstrap resampling method, are included in Table S3 of the Supporting Information.

The final variable set for the h -O(2p) prediction model includes only three variables describing the effective charge of the metals coordinated along the O–M–O chain: avg. ox, channel CI, and chain CI. The average oxidation state of the metals is inversely correlated to the energy of the h -O(2p) state (left panel of Figure 4), as characterized by a negative weight on the avg. ox variable in the h -O(2p) prediction model. For the same reason, increasing the number of CI's, which signifies a decrease in the metal ion oxidation state, increases the energy of the h -O(2p) state. Therefore the channel CI and chain CI variables are both directly correlated to the h -O(2p) energy.

The avg. ox, channel CI, and chain CI variables are also included in the final variable set of the CB prediction model. The oxidation state of a metal is directly related to the amount of octahedral splitting, Δ_o . As the splitting is increased, the t_{2g} orbital energies are lowered. Because t_{2g} d-orbitals are generally the states positioned at the bottom of the CB, this corresponds to a decrease in the CB energy (Figure 3). Therefore the avg. ox variable is inversely correlated to the energy of the CB, whereas the channel CI and chain CI variables are directly correlated. On the other hand, the value

(43) Geladi, P.; Kowalski, B. R. *Anal. Chim. Acta* **1986**, *185*, 1.

(44) Eastment, H. T.; Krazanowski, W. J. *Technometrics* **1982**, *24*, 73.

(45) R Development Core Team. *R: A Language and Environment for Statistical Computing*; R Foundation for Statistical Computing: Vienna, Austria, 2007.

(46) Efron, B. *The Jackknife, the Bootstrap and Other Resampling Plans*; Capital City Press: Montpelier, VT, 1982.

of Δ_O is known to be indirectly related to the ionic radius of a metal (section 3.1.2), so that the avg. IR variable is directly related to the CB energy. The energy of the CB is also correlated with the number of occupied d orbitals in the system. The occupation of d-orbitals lowers the energy of the occupied d states as well as the unoccupied d-states. Therefore the CB energy is lowered with an increasing number of d-electrons.

Similar to the CB, the energy of the $M_i(d_{xy})$ states is also dependent on the t_{2g} d-orbital energies of a given metal. Therefore the M_i IR and M_i ox variables are strongly correlated to the energy of these localized $M_i(d_{xy})$ states. The oxidation states of the other metals in the system are also found to be important in predicting the energy of the localized $M_i(d_{xy})$ state for a given metal. As the oxidation state of the other metals decrease, additional CI's are needed for charge neutrality. This changes the overall effective charge of the metal site in question. Interestingly, the variables describing the local and complete CI environment are not required for the $M_i(d_{xy})$ prediction. This suggests that the information included in the oxidation states of the metal in question, as well as the oxidation states of the neighboring metals are enough to predict the effective charge on a specific metal site.

The $M_i(d_{xy})$ prediction model also includes variables involving d-electrons. As higher energy d orbitals become occupied in a given M_iO_6 system, the energy of the $M_i(d_{xy})$ state is lowered. Therefore the total number of d-electrons that a given metal M_i contributes is indirectly related to the energy of its $M_i(d_{xy})$ state. Of all the occupied d-orbitals, however, the occupation of the $M_i(d_{xy})$ orbitals weighs the most heavily on the energy of this state. The coefficient for the M_i-d_{xy} occ. variable (see Table S3 in the Supporting Information), shows that on average, the energy of the $M_i(d_{xy})$ state is lowered by ~ 0.5 eV upon occupation.

Finally, the position of a transition metal ion along the O–M–O chain is identified as an important variable in predicting the resulting $M_i(d_{xy})$ energy for a given metal. In general, metal ions substituted into the bulk position have lower $M_i(d_{xy})$ orbital energies due to shorter M–O_a and longer M–O_{eq} bond lengths as well as an increased effective charge. The $M_i(d_{xy})$ model predicts that on average the d_{xy} energy for a given metal will decrease by ~ 0.25 eV if it is substituted into a bulk site versus a surface site (see Table S3 in the Supporting Information).

3.2.3. Prediction Error. Included in Table S3 in the Supporting Information are the bootstrapped mean RMSEP values for the final prediction models as estimated by the PLS regression. The 90% confidence intervals for each orbital energy prediction are estimated using a t-value of 1.646 (Figure 5). At this level all orbital energies are known to within ± 0.4 eV. We are also able to estimate the prediction error for a given optical transition using

$$\sigma_{\text{transition}} = \sqrt{\sigma_{\text{initial}}^2 - \sigma_{\text{final}}^2} \quad (1)$$

where $\sigma_{\text{transition}}$ is the standard deviation of the transition and σ_{initial} and σ_{final} are the standard deviations for the initial and final states. The 90% confidence intervals for the optical

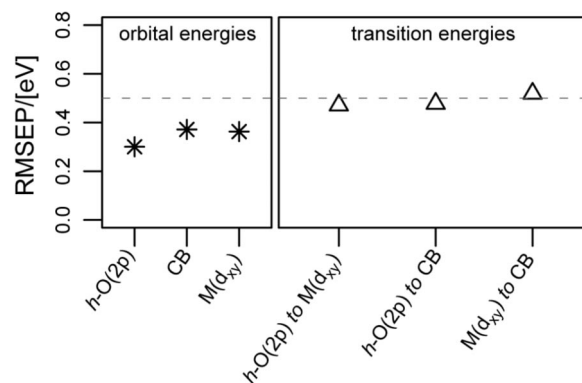


Figure 5. RMSEP values at the 90% confidence interval for the orbital energies, T, and the optical transition energies, Δ . At this level, all optical transitions are known to within ± 0.5 eV including the lowest LMCT transition energy ($h\text{-O}(2p) \rightarrow \text{CB}$ transition).

transitions are shown in the right-hand side of Figure 5. All optical transition energy predictions are accurate to within ± 0.5 eV, including the prediction of the lowest LMCT energy ($h\text{-O}(2p) \rightarrow \text{CB}$).

We have employed cross-validation on all prediction models demonstrating the robustness of the PLS predictions. For brevity, the cross-validation analysis is described in detail in the Supporting Information, section S2.4 and Figure S1.

3.3. Application: Optimal Combinations of Metal Substitutions. These prediction models may be used as a first step in identifying the most likely transition metal combinations for improving the photocatalytic properties of ETS-10. We have therefore performed an analysis on all 288 unique three-metal center combinations of the eight transition metals studied here: Ti^{IV} , V^{V} , Mo^{V} , Nb^{V} , V^{IV} , Cr^{III} , Fe^{III} , and Cu^{II} . For each combination, the $h\text{-O}(2p)$, CB, and three $M_i(d_{xy})$ orbital energies were calculated using the bootstrapped coefficients weights (see Table S3 in the Supporting Information). Electron and hole trapping sites have been identified in the unique combinations as any state >0.5 eV away from the predicted $h\text{-O}(2p)$ and CB energies. The unique combinations were divided into four categories: (1) models predicted to have no charge trapping states, denoted “none”, (2) models predicted to have only hole traps, denoted h^+ , (3) models predicted to have only electron traps, denoted e^- , and (4) models predicted to have both electron and hole traps, denoted e^-/h^+ . The three unique transition metal combinations with the lowest LMCT energies, E_{LMCT} , for each of the four categories are listed in Table 1. Although ground-state DFT calculations are known to underestimate the band gap of semiconductors systematically,^{47,48} it has been shown that accurate excitation energies can be calculated with functionals using exact exchange in conjunction with time-dependent DFT (TDDFT).^{49,50} Yet, for the systems in the present study key optical transitions, such as the band gap, are preceded by numerous lower-energy transitions involving midgap states. This requires, in many cases, the convergence of more than 20 excited states and a substantial computational cost to calculate ligand to metal charge transfer

(47) Perdew, J. P.; Zunger, A. *Phys. Rev. B* **1981**, 23, 5048.

(48) Perdew, J. P.; Levy, M. *Phys. Rev. Lett.* **1983**, 51, 1884.

(49) Cavillat, V.; Champgane, B. *Chem. Phys. Lett.* **2002**, 354, 449.

(50) Dierksen, M.; Grimme, S. *J. Phys. Chem. A* **2004**, 108, 10225.

Table 1. Predicted Electronic Structure Energies^a for Selected Three-Metal Combinations Substitution in the O–M–O Chain of ETS-10

category	model			E_{LMCT}^* (eV) ^b	avg. IR (pm)	avg. ox	number of CI's	
	M1	M2	M3				channel	chain
none	V(V)	V(V)	V(V)	1.96	54.00	5.00	0	3
none	V(V)	Fe(III)	V(V)	2.34	54.33	4.33	0	5
none	V(V)	V(V)	Fe(III)	2.34	54.33	4.33	0	5
h^+	V(V)	V(IV)	V(V)	2.34	55.33	4.67	0	4
h^+	V(V)	V(IV)	Fe(III)	2.72	55.67	4.00	0	6
h^+	V(V)	Fe(III)	V(IV)	2.72	55.67	4.00	0	6
e^-	V(V)	V(V)	Ti(IV)	2.50	56.33	4.67	0	4
e^-	Nb(V)	V(V)	V(V)	2.51	57.33	5.00	0	3
e^-	V(V)	Fe(III)	Ti(IV)	2.88	56.67	4.00	0	6
e^-/h^+	Fe(III)	V(V)	V(IV)	2.72	55.67	4.00	0	6
e^-/h	Cr(III)	V(V)	V(V)	2.72	56.67	4.33	0	5
e^-/h	Mo(V)	V(V)	Fe(III)	2.72	56.67	4.33	0	5

^a A complete list of predicted electronic structure energies can be found in Supporting Information, Table S4. ^b Adjusted LMCT energy estimated using the linear correlation from ref 38 between the ground-state orbital energy difference and the more accurate TDDFT excitation energy given in eq 2.

(LMCT) transitions. Shough et al.³⁸ have previously identified a linear correlation between the excitation energy calculated from the PBE DFT ground-state orbital energy differences [$E(\text{unocc.}) - E(\text{occ.})$] and the corresponding excitation energy calculated with the more accurate and computationally demanding PBE0/TDDFT method (EE_{TDDFT}) for the ligand to metal charge transfer (LMCT) transitions using

$$EE_{\text{TDDFT}} = 1.3[E(\text{unocc.}) - E(\text{occ.})] + 0.03 \quad (2)$$

This method has been employed in the present study to estimate the LMCT energies of the transition metal combinations. These extrapolated values are included in Table 1 as E_{LMCT}^* along with key properties of the structures. A complete list of all predicted energy values for these systems can be found in Table S4 in the Supporting Information.

The combinations in Table 1 all have E_{LMCT}^* significantly lower than the experimental band gap of ETS-10 (4.03 eV), and are predicted to be within the visible range of the spectrum. Note, these combinations have an avg. ox ≥ 4 such that no channel CI's are required, and 6 or fewer chain CI's are present. Additionally, E_{LMCT}^* increases with increasing avg. IR, so that the majority of these combinations involve the smallest metal ions, V^V and Fe^{III} , where the smallest E_{LMCT}^* is observed for the all- V^V combination having no predicted charge trapping sites. The h^+ transition metal combinations contain a mix of V^V , V^{IV} , and Fe^{III} with the predicted d_{xy} hole localized on the V^{IV} center. The e^- models also include V^V and Fe^{III} as well as some higher oxidation state metal ions (Nb^V) and Ti^{IV} metals, where the predicted d_{xy} electron trap is localized on the V^V center. Finally, the e^-/h^+ models contain a mix of V^V , V^{IV} , Fe^{III} , Cr^{III} , and Mo^V , where the predicted d_{xy} electrons are localized on the V^V centers and the holes are localized on the V^{IV} , Cr^{III} , and Mo^V centers. Although the occupied $Fe^{III}(d_{xy})$ orbital is too low in energy to participate in hole trapping, Fe^{III} substitution is predicted to introduce numerous localized and delocalized electron and hole trapping states (Figure 3). Therefore, for the transition metal combinations incorporating Fe^{III} , additional charge trapping states may be possible. Note that many of the charge trapping states identified in these models are high lying (~ 0.5 eV away from the CB or VB) and therefore their assignment is less certain. We emphasize

that these predictions are intended to direct higher-level computational and experimental analyses and are used only as a first step in identifying those transition metal combinations, which may lead to possible charge trapping states.

Not all of the combinations, however, are structurally feasible. For example, we have previously identified long chains of V^V to be structurally unstable because of small V^V –O bonds and the removal of a large number of counterions.⁴⁰ Similarly, many of the transition metal combinations listed in Table 1 are likely to be structurally unstable because of the small M–O bonds of V^V and Fe^{III} and the removal of counter-ions required for V^V and Mo^V substitution. The prediction models are limited to three-metal systems only. At lower concentrations of these transition metal substitutions (i.e., with a partial concentration of Ti^{IV}) the ETS-10 structure may be stabilized while still displaying similar electronic structures. Future studies, incorporating longer chain-lengths models, would therefore be useful to more accurately predict the effects of these transition metal substitutions at lower concentrations.

As stated previously, electron and hole trapping states can improve photocatalytic activity by increasing charge separation. However, in most cases, these sites lead to recombination centers that increase the rate of electron/hole pair recombination and reduce the photocatalytic activity. Therefore the impact of the charge trapping sites in the e^- and h^+ models is uncertain. Yet in some cases, the presence of both types of charge trapping sites may actually help improve the charge separation if the two sites are separated (i.e., not in adjacent sites). In all of the e^-/h^+ models shown in Table 1, the electron and hole traps will be nearest neighbors, likely leading to an increased rate of electron–hole pair recombination. However, if these transition metals are substituted at lower concentrations there may be an increased separation between the electron and hole trapping sites, thus decreasing electron/hole pair recombination and increasing the overall photocatalytic activity.

It would also be valuable to be able to identify transition metal combinations that lower the energy of E_{LMCT}^* without incorporating any charge trapping sites. All of the models grouped into the none category in Table 1 are structurally unfeasible. Incorporating these metals at lower concentrations, however, would increase the potential for charge

trapping sites, as the incorporation of higher energy Ti^{IV} d-orbitals will raise the energy of the CB. This makes the identification of potential models with low E_{LMCT}^* and no charge trapping sites difficult. Of all of the unique three-transition metal combinations considered, the $Nb^V-Fe^{III}-Ti^{IV}$ model is predicted to lower the E_{LMCT}^* of ETS-10 by ~ 0.6 eV and contain no d_{xy} charge traps within the band gap. Additionally, the avg. ox of this model is 60 ppm, similar to the avg. ox of ETS-10 (61 ppm), suggesting that it is structurally feasible. Therefore, it may be worthwhile to apply higher-level computational and experimental analyses on this system to determine if the band gap of ETS-10 can be reduced without incorporating charge trapping sites.

4. Conclusion

Electronic structure trends have been identified for transition metal substitution into the one-dimensional O–M–O chain structure of ETS-10. Linear combinations of the key factors affecting these trends have been developed allowing predictions of the LMCT energy of most three-metal combinations to within ± 0.5 eV with 90% confidence. The linear models are also able to predict the energy of localized $M(d_{xy})$ states that may result in charge trapping sites.

The LMCT energy is estimated from two electronic energy prediction models; the highest occupied O(2p) state, $h-O(2p)$, and the state at the bottom of the conduction band. These models contain variables describing the counterion (CI) environment surrounding the O–M–O chain as well as an averaged variable for the oxidation states of the three metals in the combination. The CB model also contains an additional averaged variable describing the ionic radii of the three metal ions and the total number of d-electrons in the system.

In the one-dimensional O–M–O chain structure, mixing is not allowed between the d_{xy} orbitals of neighboring metal (M) sites resulting in n localized $M(d_{xy})$ orbitals for a chain containing n metal ions. The energies of these states are primarily governed by the d-orbital energies and local MO_6 geometry of a given metal, so that the linear models predicting these energies are heavily weighted by properties of the given metal, including oxidation state, ionic radii, number of d electrons and occupation of the d_{xy} state. The distribution of oxidation states throughout the chain also has a significant impact on the energies of the states and therefore the averaged oxidation states of the other metals in the chain are included variables.

These prediction models were used to investigate the band structure of all possible three-metal combinations for the following transition metals, Ti^{IV} , V^V , Nb^V , Mo^V , V^{IV} , Cr^{III} , Fe^{III} , and Cu^{II} . The results indicate that systems with small ionic radii (V^V , Fe^{III}) and high oxidation states (V^V , Mo^V)

are favored for obtaining low LMCT energies within the visible range of the spectrum. However, the ETS-10 structure cannot accommodate long chains of small ionic radii and/or high oxidation state metals. Therefore, a fraction of transition metal ions with large ionic radii and higher oxidation states must be included for structure stabilization.

In general, the transition metal combinations with the lowest predicted LMCT energies, have d_{xy} electron traps localized on V^V centers and d_{xy} hole traps localized on V^{IV} , Mo^V , and Cr^{III} centers. Fe^{III} substitution may also introduce additional electron and hole trapping sites. These transition metals are therefore important for improving the charge separation in ETS-10 and thus improving the overall photocatalytic activity of the material. However, the effect of charge trapping states on the photocatalytic activity is always uncertain as these states may also serve as recombination centers, actually decreasing the photocatalytic activity. Therefore, a $Nb^V-Fe^{III}-Ti^{IV}$ model has also been identified as a possible combination which may lower the band gap of ETS-10 by ~ 0.6 eV without introducing any charge trapping states.

Although these prediction models are fine-tuned to the unique structure of ETS-10, this study has identified important electronic structure trends that occur upon transition metal substitution into a one-dimensional chain structure. The localization of the $M(d_{xy})$ orbitals is likely to exist in similar one-dimensional structures, leading to possible localized charge trapping sites. In the development of the linear models we have identified a methodology that can be applied to search all possible transition metal combinations exhaustively as a first estimate to identify key combinations that may improve the overall photocatalytic activity of ETS-10.

Acknowledgment. This research was supported by the U.S. Department of Energy under Grant DE-FG02-07-ER15921.

Supporting Information Available: Details on computational methods for investigation of structural model; table reporting the M–O bonds for the optimized structural models; details on the development of the methods used to develop and validate the linear prediction models, including a table of the 30 3 M ONIOM models and their predicted $h-O(2p)$, CB, and $M_i(d_{xy})$ energies, a list of the 19 initial variables considered for the linear models, parameters used in bootstrap resampling, criteria used to identify the final variable set, and a description of the cross-validation methods and analysis; table reporting the final coefficient weights and standard deviations and RMSEP values for the linear prediction models; an extended version of Table 3, reporting all of the predicted electronic structure energies for the selected three-metal combinations (PDF). This information is available free of charge via the Internet at <http://pubs.acs.org>.

CM8021177